Journal of Manufacturing Processes 125 (2024) 283–294

Contents lists available at ScienceDirect

Journal of Manufacturing Processes

journal homepage: www.elsevier.com/locate/manpro

Study of dynamic behaviour via Taylor anvil test and structure observation of M300 maraging steel fabricated by the selective laser melting method

Stepan Kolomy, Miroslav Jopek *, Josef Sedlak, Marek Benc, Jan Zouhar

Brno University of Technology, Faculty of Mechanical Engineering, Brno, Czech Republic

ARTICLE INFO

Keywords:
Maraging steel
Taylor anvil test
Selective laser melting
Johnson–cook
High strain rate
Microhardness
Structure

ABSTRACT

This paper deals with the M300 high strength maraging steel fabricated via selective laser melting method. Mechanical properties especially microhardness and compressive yield strength of maraging steel in as-printed state were observed. The acquired data was implemented in Johnson-Cook constitutive equation used for numeric simulation, which showed the satisfactory correlation with the observed experiment. Dynamic behaviour under high strain rate (impact velocity reached 185 $m.s^{-1}$) was investigated via Taylor Anvil Test. The experiment revealed structure and geometrical changes accompanied with the creation of characteristic funnel-like and cylindrical areas on the deformed sample. Impacted sample forehead featured the increase of microhardness (465 HV) accompanied with structure changes. The structure in the funnel-like area exhibited the decrease of average grain size, which reached the minimum (3.1 μm) in the vicinity of the impacted forehead. Closer analysis revealed that the high strain rate caused the increase of high fraction high-angle grain boundaries (50,8 %) and higher geometrically necessary dislocation density (52.77 $1.m^{-2}$) in the funnel-like area.

1. Introduction

Additive manufacturing (AM) is the process of creating a part based on a digital model created via Computer Aided Design (CAD) software. In AM, material is gradually added (layer by layer), while in machining, material is gradually removed. The part is finally formed by sintering individual layers of a defined thickness, which are stacked on top of each other [1]. This technology enables production of complex shapes that would not be possible to produce by conventional methods [2,3]. AM is used and represented in several sectors such as the automotive and aerospace industries. It could also find its application in healthcare and fashion [4–6]. AM enables to manufacture various types of materials, such as tool steel [7] stainless steel 15-5PH [8] and 316 L steel [9–11], Inconel 718 [12–14], Ni alloy [15], Ti alloy [16,17] or Al alloy [18,19], whose structure and mechanical properties can differ depending on the printing parameters, strategies, heat treatment, etc. [20,21].

Generally, the behaviour of most materials under dynamic loading is different than under static/quasi-static loading [22,23]. Machine components such as gearboxes, crankshafts etc. are subjected to dynamic loading decreasing their life. The use of dynamic tests provides a material assessment, which helps to design new components. Dynamic tests will obtain inputs into the material models, which can be used for numeric simulation. The simulation provides real results, which can be used in the design of machine components. The methods, which can be used to evaluate dynamic properties of the material are the Split Hopkinson Pressure Bar (SHPB) method and the Taylor Anvil Test (TAT) often performed to gain hardening behaviours of numerous alloys at ultra-high strain [24]. TAT can also be used in reverse mode to evaluate the response of the material to dynamic loading or can be used in ballistics tests [25]. Using the results of the dynamic properties in practice could lead to a better, more accurate and faster design of a machine component [26].

Many studies and articles focused on the investigation of the dynamic properties of materials. Rua et al. [27] studied composites with epoxy resin polymer matrix. The microstructure of the test samples were investigated using scanning electron microscopy. Dynamic tests of the material were performed using the SHPB test, which provided stress-strain curves for different strain rates. Lu and Li [28] investigated the dynamic behaviour of polymers at high strain rates using the SHPB. The experimentally measured dependence of stress on strain for different strain rates is subsequently implemented into the dynamic constitutive Johnson-Cook equation including the effect of strain rate and temperature. Gilbertson [29] investigated the dynamic properties of wood using the SHPB. The deformation of the sample was measured by strain

* Corresponding author.
E-mail address: jopek@fme.vutbr.cz (M. Jopek).

https://doi.org/10.1016/j.jmapro.2024.07.057
Received 21 March 2023; Received in revised form 15 April 2024; Accepted 10 July 2024
Available online 20 July 2024

gauge and digital image analysis. SHPB has been found to be a useful tool for assessing the material properties of wood subjected to high strain rates for short loading times. Chen et al. [30] investigated the dynamic properties of specimens made from concrete. Testing was performed using The SHPB for different loading angles and different impact velocities. For lower impact velocities, the stress-strain curve featured a similar course to quasi-static loading, in which the initial crack occurs in the centre of the specimen and propagates outward. Impact velocity has a significant role in terms of local stress distribution in the sample. Kang et al. [31] compared the dynamic properties of shale and granite. Dynamic properties were evaluated using SHPB. They found that dynamic loading reduced the impact strength. Renliang et al. [32] investigated the dynamic behaviour of sandstone via the SHPB. The temperature of the samples was maintained at −15 °C during the experiment. The test results revealed that when the average strain rate was low, the sample strength changed gradually but when it was high, its strength changed rapidly. Li, Xu, Chen et al. [33] investigated the dynamic properties of coal samples subjected to different impact velocities. They observed an obvious strain rate effect on the dynamic strength of specimens, which exhibited cracks under defined impacted angle, affecting stress concentration in specimens and changed their dynamic behaviour.

High demands on the high-series production of such components, which are typically manufactured from Fe material by automatic sequential machines, which can produce components at strain rates up to 10^3 s^{-1}. To ensure successful industrial production the mapping of dynamic behaviour of the used material is critical. Liu et al. [34] used SHPB for the investigation of U71Mn steel (used for rails) the dynamic properties over a wide range of strain rates and temperatures. Johnson-Cook models were determined regarding this material based on the experimental data. Jopek [35] investigated the dynamic behaviour of TRISTAL low carbon steel using the TAT. The experiment was performed on a device in the laboratory of high deformation rates at the Faculty of Mechanical Engineering in Brno. The LS DYNA program was used to simulate the mechanical behaviour of TRISTAL steel under dynamic loading. Kuncicka et al. [36] showed the results of the important parameters implemented in Johnson-Cook constitutive equation of TRISTAL steel. Numeric simulation confirmed a satisfactory correlation with experimentally observed data.

The study of dynamic behaviour of materials produced by the 3D printing method have been addressed by several studies. Zhang et al. [37] investigated the dynamic properties of 3D-printed ceramics. Due to different structures of AM part compared to traditionally manufactured the differences in dynamic behaviour was observed. Sharma et al. [38] investigated the effect of printing parameters on the dynamic behaviour of polyamide samples produced by the selective laser melting (SLM) method. Storage modulus increases as the laser power, bed temperature and scan length increased while it decreased with the increase in the scan spacing. Mansour et al. [39] investigated the dynamic properties of PLA material samples produced via FDM technology. A few samples were reinforced with graphene and subsequently subjected to dynamic tests. The results showed that the incorporation of graphene improved the elastic modulus, strength, and hardness of the 3D printed samples. Studies [40,41] investigated the dynamic behaviour of Ti-6Al-4 V samples fabricated by AM. The results obtained through numeric simulation showed a linear relationship with experimentally obtained results. Dynamic-mechanical properties of AM AlSi10Mg aluminium alloy were investigated via SHPB to gain stress-strain curves. Differences in the dynamic properties of this alloy produced with different material orientations accompanied with anisotropic properties were observed [42–44]. A series of TATs were performed on additively (by SLM) and conventionally manufactured 316 L stainless steel samples. A difference in dynamic properties was observed between vertical, horizontal (SLM) and conventionally manufactured specimens [45,46]. Researchers [47,48] tested AM as-built maraging steel specimens, which were subjected to dynamic loadings to investigate the dynamic behaviour, deformation mechanisms, microstructural and texture evolution via SHPB. Results showed, as-built samples exhibited fracture at the strain rate of 3500 s^{-1}.

Maraging steel produced by AM is not perfectly known in regard of the dynamic behaviour. Not many existing studies were focused on dynamic investigation of M300 maraging steel fabricated via SLM. The aim of this study is to analyse the dynamic behaviour of M300 maraging steel via Taylor anvil test. Mechanical properties especially compressive yield strength and microhardness in as-printed state were evaluated to gain the information about the material model, which is implemented into the Johnson-Cook constitutive equation and subsequently used for numeric simulation. The Real experiment is accompanied with the following analysis revealing a severe structure change. Crystallographic texture, average grain size, high angle grain boundaries and geometrically necessary dislocation density are described in detail.

2. Experimental procedure

Metal powder of the M300 maraging steel was used to produce the samples. Four various types of samples, which were used for different types of analysis were fabricated (types of samples are listed in Table 1). Furthermore, the chemical composition of as-printed sample (type 1) was determined using the Q4 TASMAN (Bruker, Rudice, Czech Republic) device. The gained chemical composition of this sample (presented in Table 2) complied with the virgin chemical composition of powder provided by the producer. Cylindrical samples for testing were fabricated using the RENISHAW RenAM 500E (RENISHAW, New Mills, UK) 3D printer. Meander Hatching Patten strategy with 67° rotation after each layer was used for fabrication of the samples (see Fig. 1a). The strategy provides sufficient melting process, which exhibits low porosity and formation of a favourable structure [49]. Sample porosity (type 2) was evaluated by optical microscope Olympus DSX500, which was used to scan the surface of the sample. The building direction (BD) was directed to the Z axis (vertical direction). Process parameters used for fabrication are listed in Table 3. The eq. (1) [50,51] was used for the calculation of the energy density, which was set during the building process.

$$E = \frac{\mathrm{P}}{\mathrm{vht}} \tag{1}$$

where E is laser energy density (J.mm^{-3}), P is laser power (W), v is scanning speed (mm.s^{-1}), h is hatch spacing (mm) and t is layer thickness (mm).

Microhardness of the samples (type 3) was measured in as-printed state. Microhardness measurement was performed in two various directions i.e. horizontal and vertical, using load of 200 g and dwell time 10s. To gain the compressive yield strength, necessary machining operation was carried out. Both faces of the sample were not perfectly flat after fabrication (there was a support on the first face and the second face was not flat). Post process face turning brought favourable surface quality on both faces. Subsequently the samples were placed into a special fixture, which was used to compressive test and were pressed at the constant speed 10 mm.min^{-1} at the room temperature 22 °C ± 1. Machine with an EDC 60 (Brno, Czech Republic) control unit was used for compressive loading. For data acquisition the TIRAtest v.2.1 software was used. Stress–logarithmic strain curves were determined from acquired data.

Table 1
Types of different samples used for different type of analysis.

Type	Analysis	state	amount [−]
1	Chemical composition	as-fabricated	1
2	Porosity evaluation	as-fabricated	1
3	Testing of mechanical properties	as-fabricated	8
4	Dynamic testing	as-fabricated	1

Table 2
Chemical composition of tested sample.

Element	Ni	Co	Mo	Ti	Si	Mn	C	P	Fe
Q4 TASMAN [Wt%]	18.38	8.84	4.67	0.71	0.01	0.04	0.02	0.02	66.40

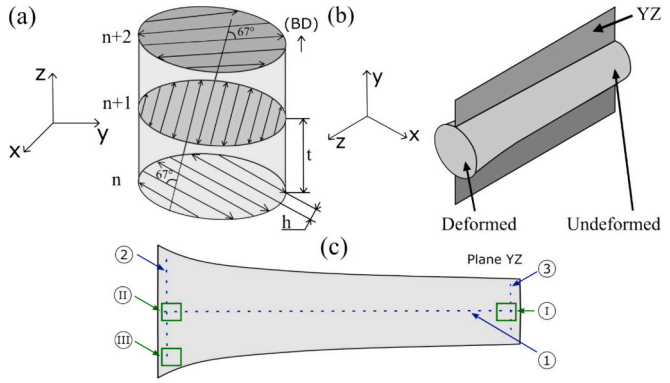

Fig. 1. (a) Meander Hatching Patten 67° rotation after each layer and (b) Cross-section plane depicted in the sample subjected to TAT and (c) lines 1–3 used for microhardness measurement and places I-III in YZ plane used for structure observation.

Table 3
Process parameters used for fabrication of the samples.

Energy density [J/mm^3]	Laser power [W]	Scanning speed [mm/s]	Laser thickness [mm]	Hatch spacing [mm]
133	410	810	0.04	0.095

Test of dynamic behaviour via TAT took place in the laboratory of high strain rates at the Faculty of Mechanical Engineering BUT in Brno. The device used for testing of the dynamic properties is shown in Fig. 2a. The sample (type 4) together with the carrier (see Fig. 2b) is placed in the air vessel from where the sample was fired towards the fixed bar. Imminently the sample was separated from the carrier, the impact velocity was measured. The impact velocity reached max. Value of 185 m. s^{-1} in this experiment. Fig. 2c shows initial dimensions of the sample

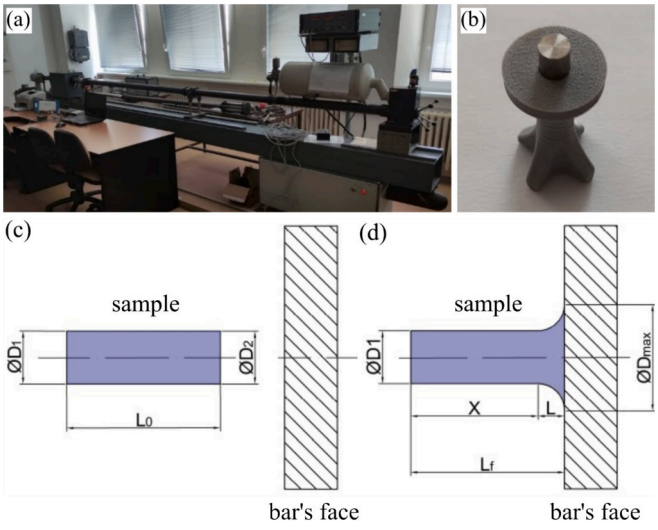

Fig. 2. (a) Device used for testing of dynamic properties via TAT, (b) assemble contains of sample and carrier and material model (c) before deformation (d) after deformation.

used for dynamic testing, where L_0 is the length of the sample and D_1 and D_2 are diameters on both sample faces. Fig. 2d represents material model with the key parameters (L_f = final length, X = length of non-deformed area, L = length of deformed area, D1 = diameter of non-deformed cylindrical area, D_{max} = max. Diameter after deformation) subsequently integrated in the numeric simulation.

Detailed structure observation of sample after TAT, which was prepared by puck casting and automatically polished and etched by 2 % nital solution was examined. Microhardness of deformed sample was measured in YZ plane (see Fig. 1b) along and perpendicular to sample axis (see Fig. 1c). The structure was observed in the YZ plane using the Olympus DSX500 (Olympus, Prag, Czech Republic) light microscope and the KEYENCE VHX-F (KEYENCE, Mechelen, Belgium) digital microscope. Tescan Lyra 3 XMU FEG/SEMxFIB (Tescan, Brno, Czech Republic) with Symmetry EBSD detector was used for detailed study of the microstructure. The scan step for the EBSD (electron-backscatter) scanning was 0.15 μm.

Numerical simulation of TAT was realised using software ANSYS Explicit dynamic (Ansys Inc., Canonsburg, Pennsylvania, USA). Hexagonal mesh was applied to evaluate the sample after TAT via finite element method (FEM). Close to 270 thousand elements with 308 thousand nodes were implemented for the detail definition, with no applied re-meshing. The starting temperature was set as 22 °C. The TAT numerical simulation was carried out using Johnson-Cook (J–C) eq. (2). Each parameter from the equation was determined experimentally and compared to parameters acquired by the numeric simulation.

$$\sigma = (\sigma_0 + B\varphi^n) \bullet \left(1 + C\, ln\frac{\dot{\varphi}}{\dot{\varphi}_0}\right) \bullet (1 - T^{*m}) \quad (2)$$

where σ_0 is static flow stress, B is work hardening coefficient, $\dot{\varphi}$ is strain rate, n is work hardening exponent, C is strain rate sensitivity, m is the thermal softening coefficient, and T* is homological temperature defined in the range $0 < T^* < 1$ by eq. (3)

$$T^* = \frac{T - T_0}{T_m - T_0} \quad (3)$$

where T_0 is the reference temperature (at static flow stress $\sigma_0 = \sigma$), and T_m is the melting temperature.

3. Results and discussions

The process of 3D printing is based on the concept of placing each layer by layer until the whole part is fabricated. Direct printed surface is depicted in Fig. 3. Fig. 3a shows the front view of the as-printed sample where the hatching paths are clearly visible. Distance between each path is approximately equal to 0.095 mm (hatch spacing). Fig. 3b shows the side view of the printed sample. This surface featured a non-sufficient surface quality after printing. The cover layer of printed samples contains plenty of micropores and voids, which can negatively affect dynamic and mechanical properties [52]. Therefore, it is needed to machine surfaces, which are considered to be functional.

AM technology especially SLM can produce nearly fully dense and high-performance parts of a very complex shape [53]. The combination of implemented process parameters could affect the forming structure and the porosity [54]. Pores, cavities, or voids could appear due to the protecting gas, which is entrapped during the sintering process [55,56]. Structure, which reports lower porosity would feature higher fatigue resistance and mechanical properties [57]. Porosity was examined on

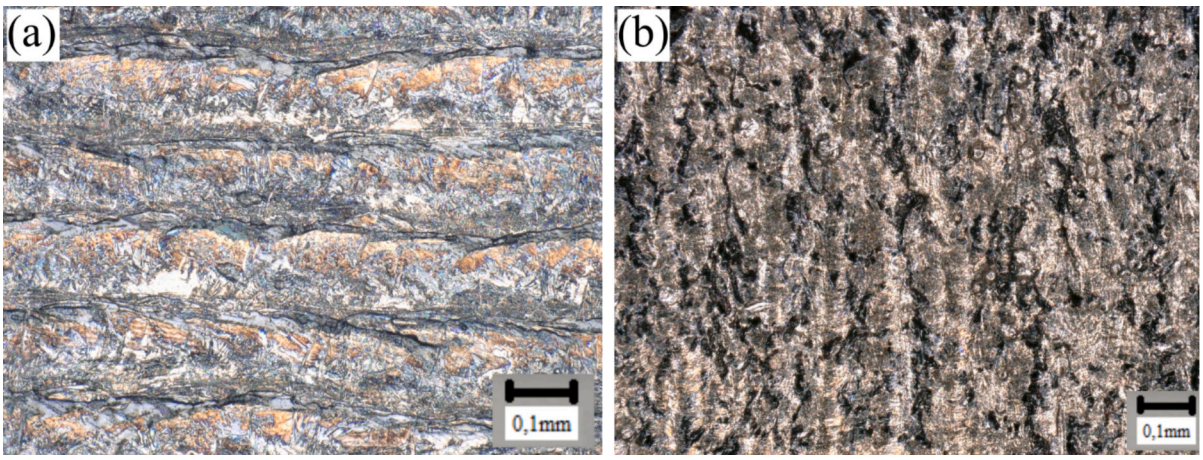

Fig. 3. Surface quality in as-printed state: (a) front view on SLM piece and (b) side view.

the sample (type 2 mentioned in Table 1), which was fabricated with identical process parameters. Porosity was evaluated in horizontal (see Fig. 4a) and vertical direction (see Fig. 4b). Three individual planes in each direction (perpendicular and parallel to BD) were chosen. The planes were situated on top, in middle height and in the bottom of the sample. These planes were separately scanned on optical microscope Olympus DSX500. Porosity of the sample is calculated as average value from each single evaluated plane (see Table 4). Fig. 4 shows the micro and macro pores, which are situated dominantly in cover layer of the sample. In case of removal the cover layer (0.4 mm from surface) the global porosity would decrease dramatically. The porosity was also evaluated without considering the cover layer, which brought the significant reduction of porosity.

3.1. Mechanical properties

The as-printed samples (type 3 corresponding to Table 1) were used for the microhardness evaluation. Four individual samples were measured to determine microhardness in horizontal (perpendicular to BD) and vertical (parallel to BD) directions, which is depicted in Fig. 5. The middle height plane was used to measure microhardness in horizontal direction due to the expectations of the highest porosity connected with lower microhardness [58]. The resulting values of microhardness are given as the average values calculated from 12 indentations in each direction. Average microhardness in horizontal and vertical direction featured to 411 HV and 410 HV respectively. It could be concluded; the microhardness is independent on its measuring direction.

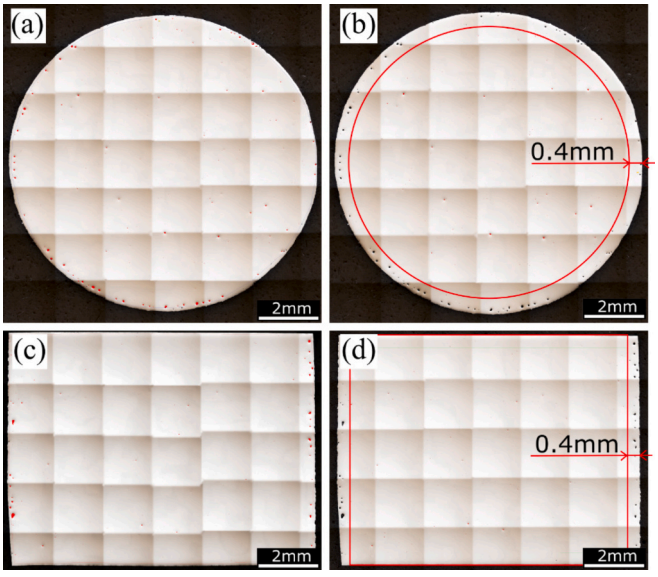

Fig. 4. Light optical microscopy (LOM) images show porosity (cross-section in middle height) in (a, b) horizontal direction and (c, d) vertical direction, (a–d) corresponds to sample type 2 according to Table 1.

Table 4
Evaluated porosity of the sample in horizontal a vertical direction.

SAMPLE Type 2	Porosity in horizontal direction [%]			Porosity in vertical direction [%]		
Section	1	2	3	1	2	3
Unbounded area	0.161	0.180	0.170	0.160	0.150	0.190
Bounded area	0.022	0.025	0.031	0.025	0.023	0.029

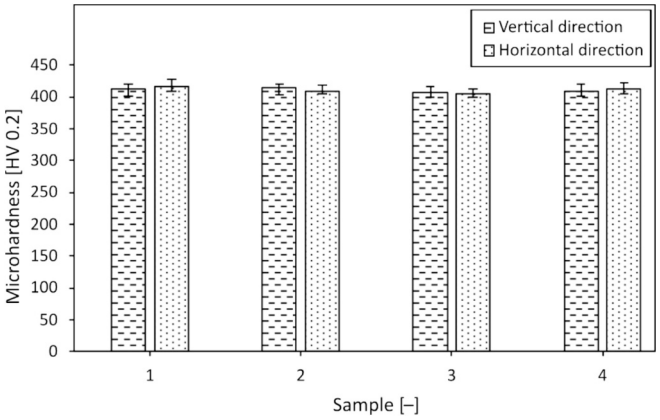

Fig. 5. Microhardness of four different samples in as-printed state. Microhardness is given in horizontal and vertical direction.

Both faces of as-printed samples (type 3) were not perfectly flat after fabrication. The first face of the sample featured a building support, and the second face did not exhibit with an appropriate surface quality. Face turning provided a favourable surface quality, which ensured the sufficient conditions for compressive testing. The compressive stress – logarithmic strain curves of the examined samples are shown in Fig. 6. The different compression stroke was applied, which varied for each sample: sample 1 featured the 6 mm stroke, sample 2 was exposed to 7 mm compression stroke, sample 3 and sample 4 were exposed to 8 mm and 9 mm compression stroke. Due to the various compression stroke the imposed logarithmic strain was different for each sample. The average

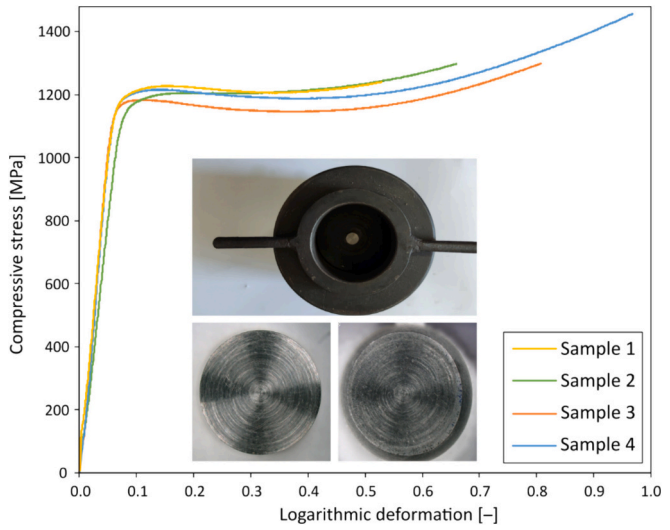

Fig. 6. Compressive stress – logarithmic strain curves of all the examined samples in as-built conditions, the sample placed in fixture and is also included.

compressive yield strength calculated from all samples featured 1177 ± 5 MPa. Additive manufactured part should withstand the higher dynamical load the higher mechanical properties, the part exhibited [59]. The final dimensions (final height, maximal and minimal diameter) of compressed samples were imputed into numeric simulation to perform dynamic behaviour.

3.2. Dynamic testing

Dynamic behaviour of the sample (type 4) was examined using the TAT device. Dimensions of tested sample in undeformed state were measured and subsequently used for final evaluation as well as the dimensions after deformation. Utilisation of acquired parameters led to evaluation of dynamic behaviour via FEM. Impact velocity was 185 m. s^{-1}, which inflicted uniform plastic deformation depicted in Fig. 7. Deformed sample can be divided in two characteristic areas i.e., funnel-like, and cylindrical area. The first area was exposed to high strain rate, which led in creation of the funnel-like area, corresponding to severe plastic deformation. The creation of funnel-like area instead of barrel (in case of compressive test) proved that the sample was exposed to high strain rate (dynamic loading) and was not influenced by the friction. The second area was defined as undeformed cylinder with the initial diameter. The fact, that any macro cracks were observed, can be attributed to low impact velocity. Higher impact velocity can cause destruction of the sample due to cracks initiation [29]. The next factor, which can affect deformation could be impurity, voids, pores etc., contained in cover layer, which can lead to crack initiation and rapid destruction of the sample [60].

The sample after high strain rate was observed via scanning electron microscopy (SEM). SEM was used to detail scan of areas containing defects on the impacted region of the sample, which is depicted in Fig. 8. The uniform plastic deformation of the sample forehead (depicted in Fig. 8a) contained a huge number of traces equally spread in whole area. Fig. 8b showing the detail area containing visible impurities marked in yellow circle within this area. In addition, they can serve as a stress concentrator, from which cracks can initiate during the mechanical as well as dynamic loading. The deformed surface contained plenty of cracks formed after the frontal impact. Close detail of crack is presented in Fig. 8c. Each crack is formed in main direction with several secondary micro scratches perpendicular to main crack.

3.3. Numerical simulation

The choice of the constitutive equation was based on several requirements involving the physical nature of the event. The J–C equation includes five parameters, where two parameters, i.e. the static flow stress and the hardening coefficient, were obtained from compressive test. The acquired results from compressive test showed that the compressive yield strength are in the range 1150 MPa to 1204 MPa. The value 1204 MPa was set in J–C constitutive equation, which was used for the TAT numeric simulation.

Fig. 9a shows the dependences between the errors (percentage differences between the experiment and the simulation in the observed areas) on the strain rate sensitivity. These curves were evaluated from the sample, which featured the 185 $m.s^{-1}$ impact speed. The percentage differences were observed in the areas of maximum sample diameter D_{max} and final length L_f. The average error reached a minimum value at $C = 0.138$. When the strain rate coefficient increase/decrease the deviation would increase. After the optimization of the strain rate sensitivity parameter C, the softening exponent m was also optimized. TAT experiments were also performed at elevated temperatures, specifically for a measured surface impact temperature of 175 °C, where the heated sample was accelerated towards the bar's face. At the bar's face, the surface temperature of the sample was recorded with a non-contact temperature meter. By comparing the contour of the sample, namely the maximum sample diameter D_{max} and the final length L_f of the sample after the experiment and optimizing D_{max} and L_f of the sample in the numerical simulation given the recorded surface impact temperature, the softening exponent m was optimized. The results of the softening exponent optimization can be seen in Fig. 9b.

The dependence of deformation strain on the logarithmic deformation was obtained (see Fig. 10) by substituting individual parameters into the constitutive equation according to J–C. The curves were plotted for different strain rates, i.e., 0.02, 1200, 3000 s^{-1}. The curve acquired by compressive test (represented by the yellow line) was also included. The observed deviation between yellow and blue lines (compressive test and J–C equation) featured the minimal deviation. The parameters

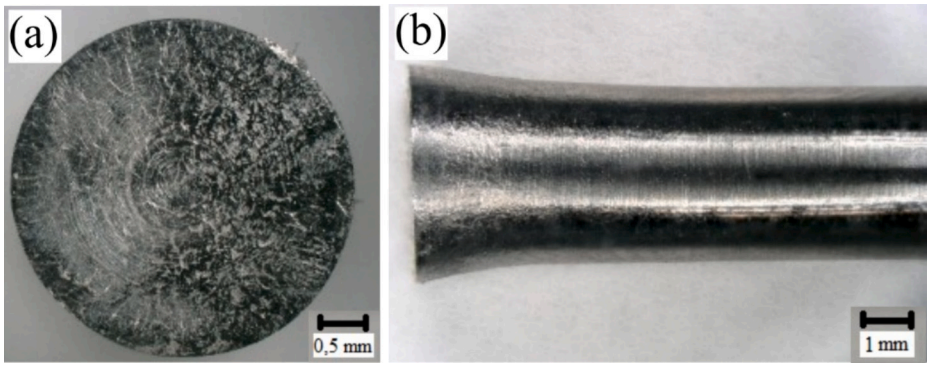

Fig. 7. Sample subjected to TAT: (a) front view of the impacted forehead of the sample, (b) side view presenting funnel-like and cylindrical area of the sample.

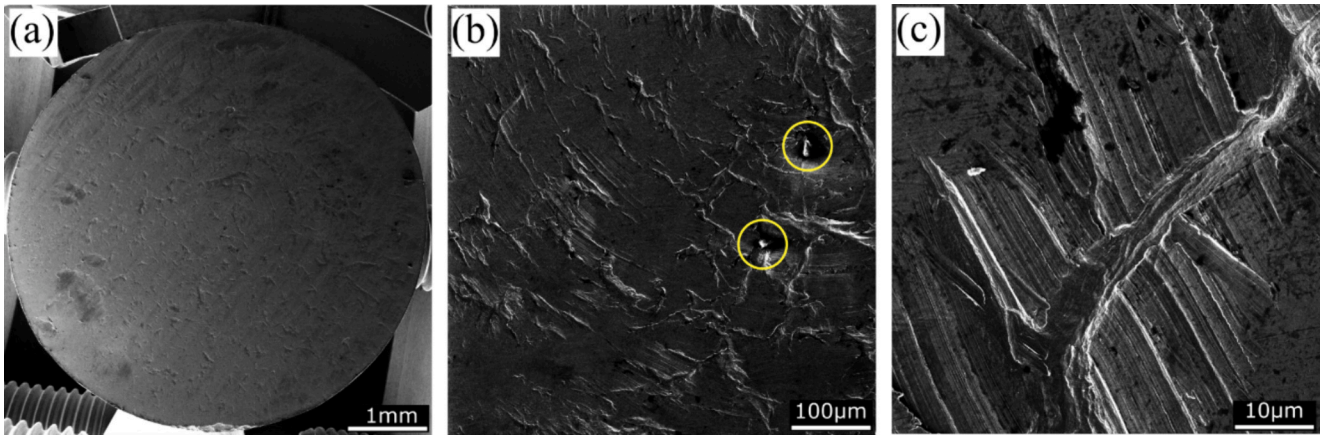

Fig. 8. SEM images of the deformed TAT sample forehead imposed to high strain rate: (a) front view of the sample, (b) area of interest, (c) detail of micro crack.

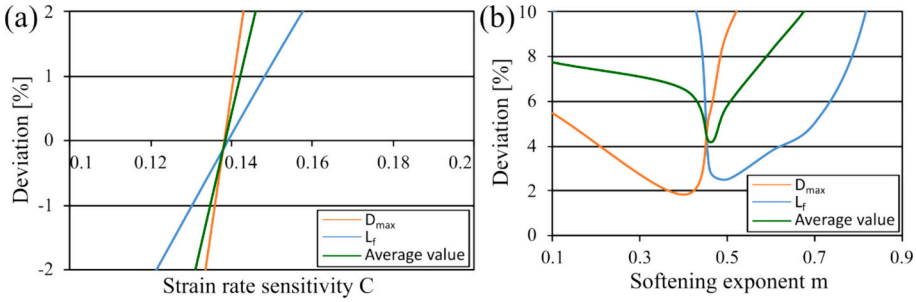

Fig. 9. Dependence of the deviation on the strain rate sensitivity (a) and dependence of the deviation on the softening exponent m (b).

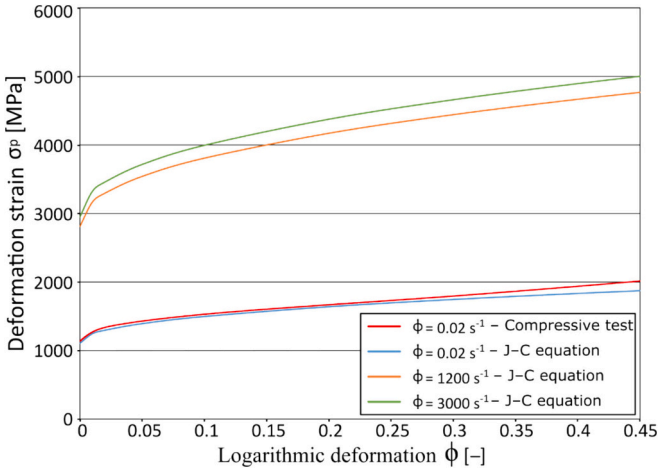

Fig. 10. Dependence of deformation strain on the logarithmic deformation.

corresponding to J–C equation, which were finally obtained by numeric simulation are shown in Table 5. The results for the effective strain, the actual strain in individual axis is depicted in Fig. 11a-d. Fig. 11a shows the distribution of XY strain components throughout the tested sample after TAT, which exhibited the highest deformation at impacted forehead. Numerically predicted distributions of the stress is depicted in

Table 5
Numerically obtained parameters of J–C constitutive equation.

σ_0 [MPa]	B [–]	n [–]	C [–]	m [–]
1104	1099	0.449	0.138	0.46

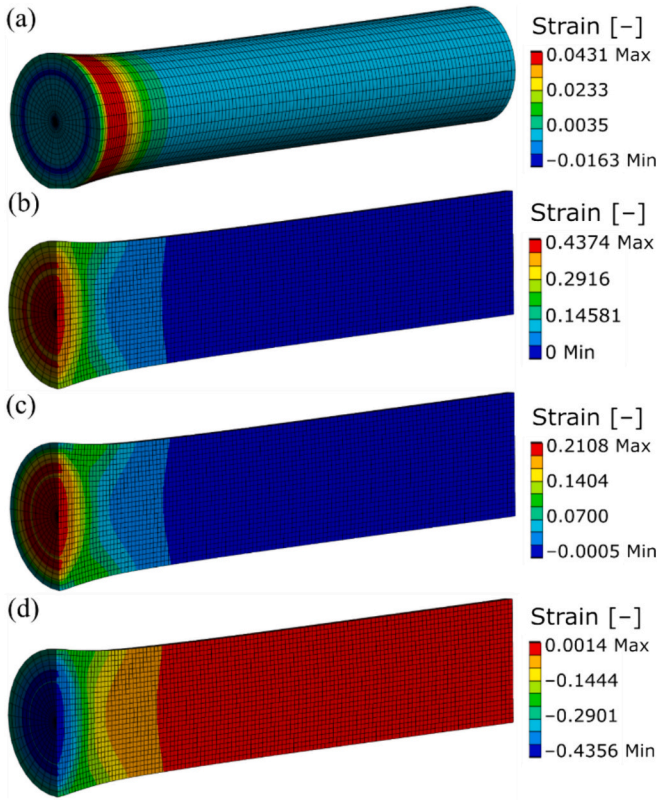

Fig. 11. Numerically predicted distributions of strain in XY (a), distribution of stress (b), YY strain (c) and XX strain (d).

Fig. 11b whereas Fig. 11c predicts the distribution of YY strain within tested sample, which reached maximum in vicinity of the centre. Fig. 11d predicts distribution of XX strain in the TAT tested sample.

3.4. Microhardness evaluation

Microhardness in deformed state after TAT was evaluated in vertical (YZ plane is depicted Fig. 1b) direction. The microhardness (according to Vickers HV 0.2) was evaluated in three individual measurements (lines 1–3 corresponding to Fig. 1c) in longitudinal and transverse direction. Microhardness in line 1 (depicted in Fig. 12a) was measured along the sample axis. A total of 193 individual indentions in 0.1 mm were performed in this line. The course of the microhardness corresponds with the contour (depicted in Fig. 12a) of deformed sample. The microhardness copies the course of the contour, which reached the highest observed value (465 HV) in the vicinity of the impacted sample forehead due to severe plastic deformation noticed in this region. This is an increase of 13,1 % within this area, compared to the sample in as-printed state. The course shows that the microhardness decreased with the increasing distance, which is probably caused due to factors corresponding with average grain size, high angle grain boundaries and dislocation density. These factors were affected by severe plastic deformation (described in Section 3.5). The evaluated microhardness oscillated within cylindrical area (increased and decreased) according to the place, where the microhardness was measured. The structure (closer view is described in following chapter) of the as-built samples featured melting pool structure with two distinct regions, which corresponds to different etching contrast (see Fig. 12A2). Darker areas presenting a tempered martensite region, which alternate with brighter areas corresponding to less extensive tempering [61]. SEM image (see Fig. 12A1) revealed a presence of fine secondary carbides within tempered area. The microhardness measurements confirmed the lower microhardness of the darker areas (T = Tempered = 393 ± 5 HV 0.2), then brighter areas of less tempered martensite (Q = Quench = 420 ± 5 HV 0.2), which can be considered as quickly quenched region. Other current work [62] discussed the fact that as each subsequent layer is deposited, the temperature increases due to heat transfer from the solidifying layer towards to the previously deposited layer. The increase of temperature may cause the tempering process in neighbouring layers (i.e., intrinsic tempering during the SLM process). Based on acquired data, the cylindrical area of as-deformed sample can be considered to have the same microhardness as the sample in as-printed state. In other words, the strain rate influenced the microhardness only in impacted funnel-like area of the sample, as well as the cylindrical area within the sample exhibited no significant changes.

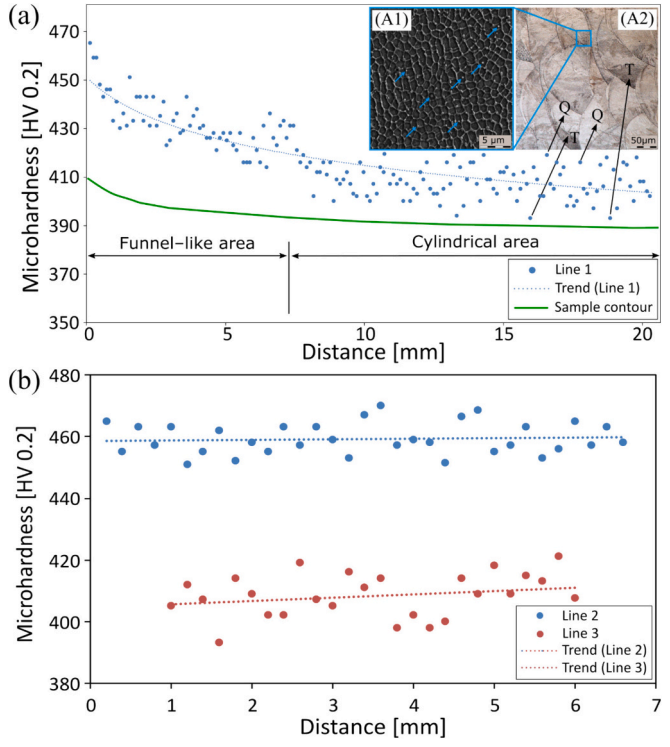

Fig. 12. Dependence of Vickers microhardness on distance in YZ plane: (a) measured microhardness in line 1, (A1) presence of fine secondary carbides, (A2) two different regions i.e., tempered, and quenched structure, (b) measured microhardness in line 2 a 3.

Microhardness in line 2 and 3 (see Fig. 12b) was measured perpendicular to the sample axis. Total of 33 and 26 individual indentions in distance of 0.2 mm were performed in these lines, where line 2 presents higher average value (459 ± 8 HV) of microhardness than line 3 (409 ± 7 HV). This is an increase of 12.2 % corresponding with geometrical and structure changes affected by severe plastic deformation, lower average grain size and high fraction of high-angle grain boundaries (HAGB, described in following chapter in detail). Considering the course of the values in each line, acquired data resulted higher dispersion in line 3 corresponding to different measured region (tempered and quench). The dispersion in line 2 was diminished due the overwhelming effect of lower average grain size, high fraction HAGB and dislocation density.

3.5. Structure observation

Fig. 13 shows a light optical microscopy image taken from the sample subjected to dynamic testing via TAT. The images represent the longitudinal cross-section in YZ plane. The structure in the cylindrical area of the sample shows (see Fig. 13a) visible scanning paths and characteristic melt pool structure typically created by the sintering process. The structure features semi-elliptical grains crystallizing in the solidifying layer, which have their longer axis perpendicular to the laser beam. The deposited layer is covered with the following scanning path creating the overlapped areas. This type of observed structure is typical for cross-section made parrallel to the building direction. SLM process causes a nonuniformal cooling rate, which is slower inside the melt pool than at the boundary resulting in a different crystallization rates and undesirable segregation inside the melting pools [63]. This segregation can affect mechanical properties of pieces produced via SLM. Due to lower set layer thickness (40 µm), it can be predicted that individual layers could be remelted several times. The remelting process can cause partial annealing of the already deposited layer resulting in nonhomogeneous mechanical properties. Structure in funnel-like area of the sample is depicted in Fig. 13b. Deformation under strain rate entailed in a change of structure. The shape of a melt pools exhibited longer main axis and shorter secondary axis compared to pools in cylindrical area resulting in change of mechanical properties.

EBSD Orientation image maps (OIMs) (depicted in Fig. 14) were constructed on images captured at 1000× magnification represent longitudinal (YZ plane) cross-section of the sample subjected to dynamic test via TAT. The grains are shown in the maps, using colours (red, green and blue) relating to their individual orientations along the three principal crystal directions i.e., ⟨001⟩, ⟨101⟩, and ⟨111⟩, according to Miller indices (the legend triangle is depicted in each figure). These orientation maps are presented on each area I-III corresponding to Fig. 1c. The grain orientations in each area were observed parallel to the building direction i.e., the longitudinal images (YZ plane) were evaluated parallel to the x axis (|| x).

Grain structure in the cylindrical area (depicted in Fig. 14a) featured mostly an irregular shape within this area I and exhibited no tendency to form in certain orientation. Grain structure depicted in Fig. 14d and g present clusters of fine equiaxed grain and few elongated grains, which can be seen legibly. Considering the OIM and orientation together, it appears that the elongated grains form perpendicular to the sample axis.

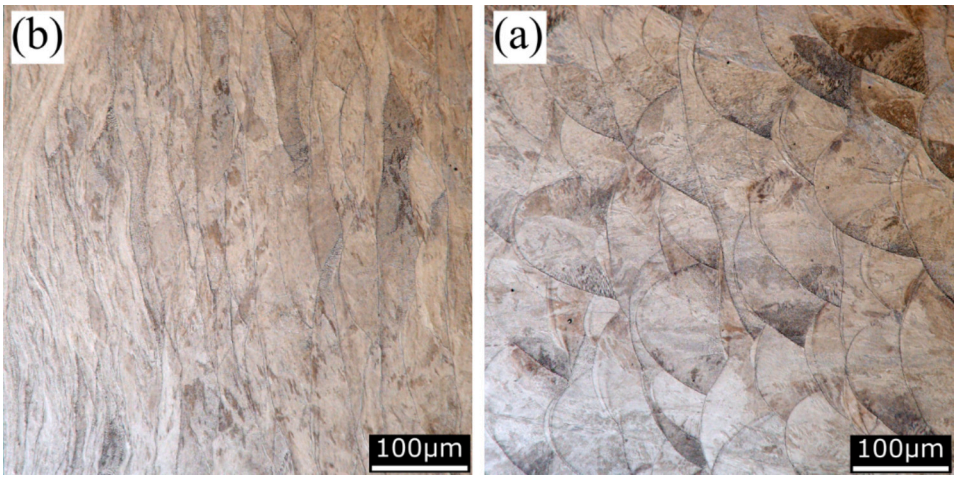

Fig. 13. Light optical microscopy (LOM) images of areas (a) I, (b) II presented in Fig. 1c.

Fig. 14d describes elongated grains in the centre of the sample, which feature a tendency to form the <101>||z preferential orientation as well as the area at the boundary of the sample (see Fig. 14g) exhibits the same tendency. Such clusters of fine equiaxed grains appear in vicinity of the impacted forehead, where the applied stress reached the maximum value. The lower impacted stress (correlate with numeric simulation) on the edge of deformed region of the sample resulted in a lower number of such clusters of fine grains. Prasad et al. [64] observed creation of the cluster of fine grains in areas which were subjected to the remelting process of successive layers.

The average grain size in all areas was examined (examination was carried out in YZ plane considering the areas I-III, see OIMs images depicted in Fig. 14a, d, g) using grain ferret diameter (defined as a maximum distance between two points within a single grain). In each area I-III the average grain size slightly varied, but the highest observed difference was among areas I and II corresponding to cylindrical and funnel-like region, respectively. Average max. Grain feret diameter in area I (cylindrical shape of the sample, which was not significantly affected with strain rate) was evaluated as 10.2 μm (the examined grain size in area I is depicted in Fig. 14b). Area II and III exhibited a structure change compared to area I. Due to strain rate a significant grain refinement was observed within areas II and III (each area II and III was chosen in funnel-like area of the sample). The average grain size decreased to 3.1 μm and 3.6 μm (see Fig. 14e and h) in area II and III respectively. This is an almost three times finer structure compared to area I (the cylindrical part of the sample).

The crystallographic texture in areas I, II, and III was studied considering the inverse pole figures (IPFs) of YZ plane. IPFs captured in area I (see Fig. 14c) featured a dominant orientation, which is formed to ⟨111⟩|| z. The crystallographic texture of the as-built sample can be affected by the energy density deposited during sintering process [65–67]. Fig. 14f and i showing characteristic IPFs for areas II and III situated in the funnel-like area of impacted forehead. Considering the IPFs of deformed region in area II, it is evident that the prevalent crystal orientation along the build direction was formed to <001>|| x orientation as well as in area III. The crystallographic texture in these areas is related rather to the impact deformation than to the sintering process. The HAGB fraction (analysis based on OIM images, threshold for a high-angle grain boundary considered to be 15) in cylindrical area I exhibited 30.6 %, which was the lowest observed fraction. The observed HAGB exhibited no significant difference in areas II and III (examined HAGB in both areas were 50.8 % and 48.2 % respectively). It is evident that after severe plastic deformation the increase of HAGB in funnel-like area of the sample was observed. However, the highest HAGB fraction was observed in the centre of the impacted forehead.

Fig. 15 shows geometrically necessary dislocation (GND) density maps estimated from the EBSD orientation data corresponding to area I-III. GNDs have been mapped in field 100 × 100 μm around grain boundaries affected by strain rate. Black pixels in each map are corresponding to non-indexed regions. Colour-scale, which is presented in each map illustrates the estimated amount of dislocation density (number of dislocations/m^2) contained within each measured pixel on the map. Fig. 15a presents acquired GND in area I, which corresponding to the lowest value of 11.25 probably due to the insufficient macroscopic stress level. The minimum GND density is in the centre of the grains with high GND accumulation in the vicinity of the grain boundaries. Grains, which showed a strong tendency to form in <101>||z preferential orientation exhibited a low GND density on these slip systems. The GND shows the highest level 52.77 in the centre of funnel-like area II (see Fig. 15b) corresponding to the highest number of high-angle grain boundaries, the lowest average grain size and to the highest observed microhardness. Fig. 15c depicts area III, where the GND decreased as well as average grain size increased compared to area II. The severe plastic deformation featured a dominant effect in the centre of the funnel-like area of the deformed sample due to creation of structure with the lowest average grain size, highest fraction of HAGB and GND density.

Based on obtained data, the microstructure and geometrical changes were influenced by high impact velocity accompanied with high strain rate. Most affected region (considering structure and geometrical shape) was the funnel-like area in the vicinity of impacted forehead of the sample. However, the cylindrical area I featured very similar microhardness compared to as-printed samples. The increase of microhardness in the funnel-like area was probably influenced by several factors: average grain size, number of dislocations and HAGB fraction. The applied impact velocity resulted in severe plastic deformation, which mainly affected the region of the deformed forehead. The average grain size decreased due to a creation of the cluster of fine grains in the vicinity of the centre sample axis. The creation of such clusters of fine grains was accompanied with forming of dislocations presented dominantly on grain boundaries. The area II close to sample axis exhibited the highest HAGB fraction, which decrease with increasing distance from the sample axis. These factors perfectly correlate with numeric simulation, which confirmed the highest observed stress in the centre area II of the sample decreasing towards area III. Mapping of the dynamic behaviour will obtain a significant data, which can be used in numeric simulations. The acquired data from compressive testing were implemented in Johnson-Cook equation used for numeric simulation. Thanks to the J-C equation new dynamically loaded components can be designed faster and more accurate (based on numeric simulation). Appropriate part surface quality is expected to increase resistance to dynamic cyclic loading as well as the final porosity of the component.

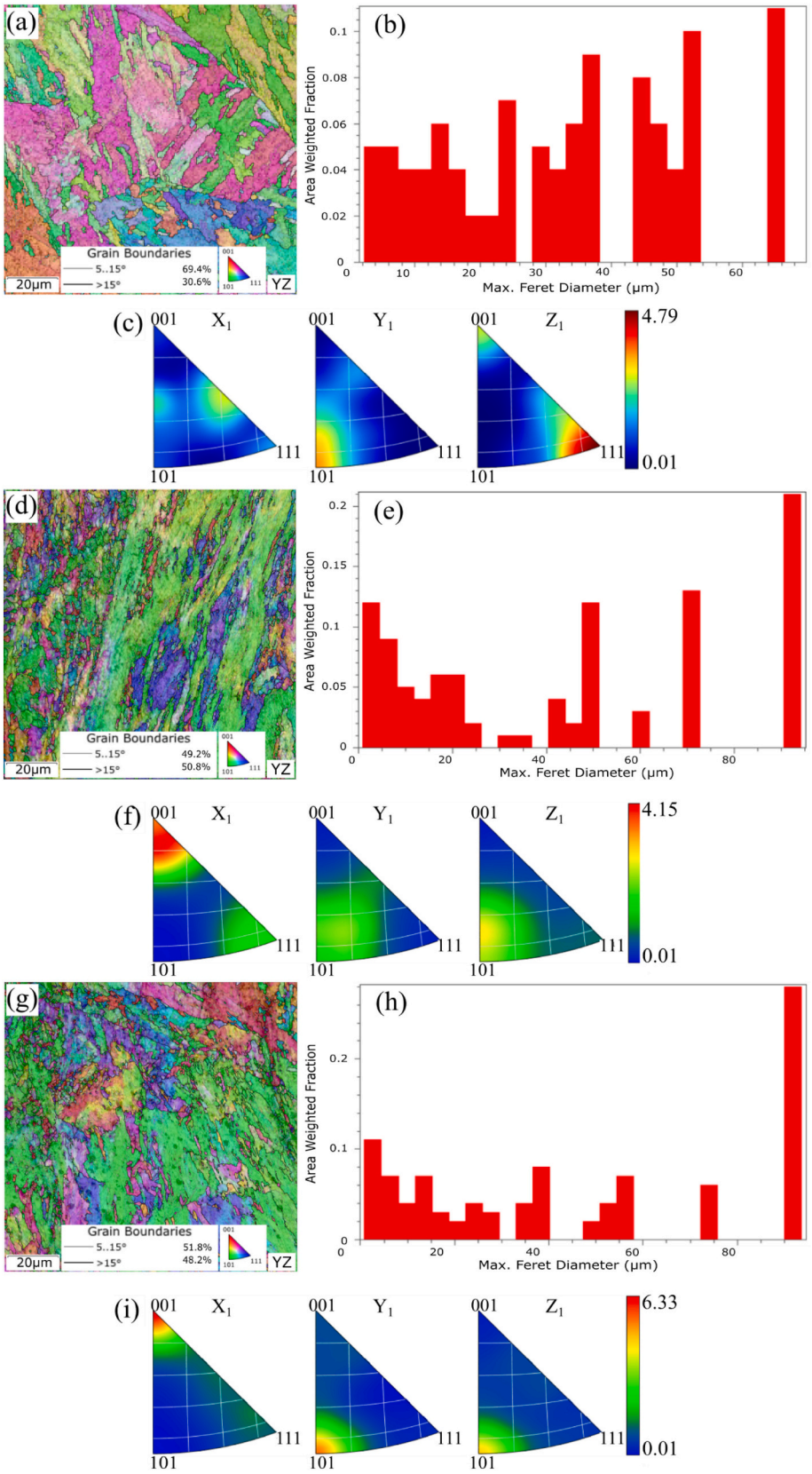

Fig. 14. OIMs of the sample subjected to dynamic test via TAT in YZ plane (a) area I, (b) max. Feret diameter in area I, (c) IPFs in area I, (d) area II, (e) max. Feret diameter in area II, (f) IPFs in area II, (g) OIMs in area III, (h) max. Feret diameter in area III, (i) IPFs in area III.

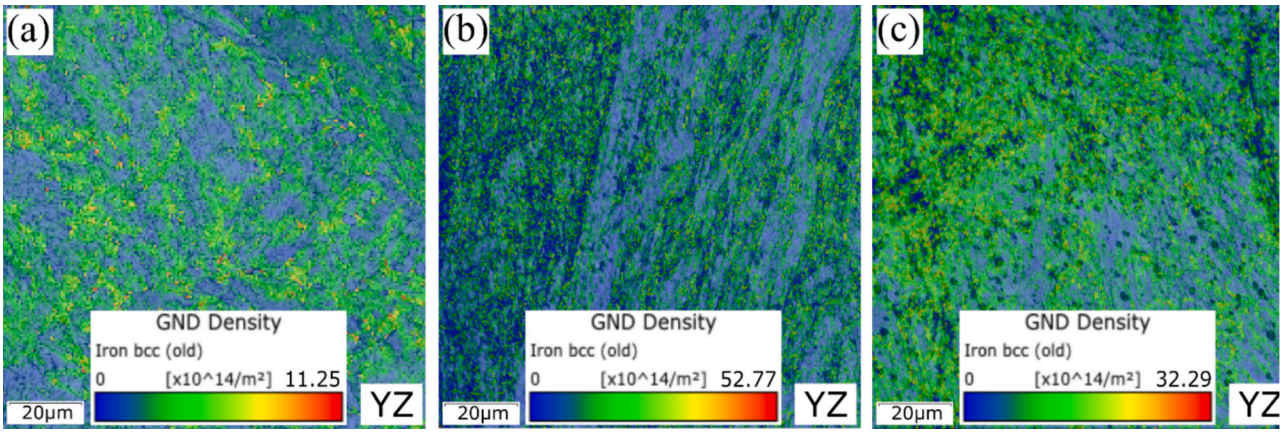

Fig. 15. GND density corresponding with areas I-III, (a) area I, (b) area II and (c) area III.

SLM process can provide parts with low porosity concentrating predominantly in cover layer. By applying post-process machining the higher surface quality corresponding with lower final porosity can be achieved. Both surface quality and porosity influence component life because any pores or microcracks situated on the component surface can initiate a crack, which very often leads to the parts destruction (especially when the part is exposed to cyclic load). The effects of post process machining (cutting speed, feed rate, type of cooling etc.) on surface quality and final porosity of additively manufacture pieces would be the focus of our following study.

4. Conclusion

In this paper, the dynamic behaviour of M300 high strength maraging steel produced by SLM via Taylor anvil test was investigated. The impact velocity of the tested sample was set to 185 m.s^{-1}, which caused the creation of characteristic funnel-like and cylindrical areas on the sample subjected to TAT. The most important conclusions revealed by the study can be described as follows:

Microhardness measured in the funnel-like area increased to 465 HV as well as the microhardness in the cylindrical area (410 HV) was not affected with high strain rate. The increase of microhardness was affected mainly with the following factors. The average grain size in the funnel-like area decreased from 10.2 to 3.1 µm in the centre of the impacted forehead of the sample. The funnel-like area featured the highest HAGB fraction, which increased from 30.6 % to 50.8 % within this area. Geometrically necessary dislocation density within the funnel-like area reached the maximum value (52.77 × 10^14 1/m^2) on the grain's boundaries observed in the centre of the tested specimen. The structure changes were influenced by the severe plastic deformation, was imparted by high impact velocity.

The study of mechanical properties in as-printed state helped to gain important parameters presented in Johnson-Cook equation, which was implemented in the numerical simulation of TAT process. The results confirmed a favourable model showing the highest observed stress in the centre of funnel-like area, which corresponded with acquired results based on structure analysis and microhardness measurement.

CRediT authorship contribution statement

Stepan Kolomy: Conceptualization, Data curation, Investigation, Methodology, Resources, Validation, Visualization, Writing – original draft, Writing – review & editing. **Miroslav Jopek:** Data curation, Investigation, Methodology, Software, Validation, Writing – original draft, Writing – review & editing. **Josef Sedlak:** Conceptualization, Formal analysis, Project administration, Visualization. **Marek Benc:** Formal analysis, Investigation, Validation, Visualization. **Jan Zouhar:** Conceptualization, Investigation, Methodology, Visualization.

Declaration of competing interest

The authors declare that they have no known competing financial interests or personal relationships that could have appeared to influence the work reported in this paper.

Acknowledgment

This research study was supported by the grant "Modern technologies for processing advanced materials used for interdisciplinary applications", FSI-S-22-7957.

References

[1] Laakso, Petri; Riipinen, Tuomas; Laukkanen, Anssi; Andersson, Tom, Jokinen, Antero et al. Optimization and Simulation of SLM Process for High Density H13 Tool Steel Parts. online. Phys Procedia. 2016, roč. 83, s. 26–35. ISSN 1875–3892. Dostupné z: doi:https://doi.org/10.1016/j.phpro.2016.08.004. [cit. 2022-07-26].

[2] Liu, Y.J; Wang, H.L; Li, S.J; Wang, S.G; Wang, W.J. et al. Compressive and fatigue behavior of beta-type titanium porous structures fabricated by electron beam melting. online. Acta Mater. 2017, roč. 126, s. 58–66. ISSN 1359–6454. Dostupné z: doi:https://doi.org/10.1016/j.actamat.2016.12.052. [cit. 2022-07-26].

[3] Kranz, J.; Herzog, D. a Emmelmann, C. Design guidelines for laser additive manufacturing of lightweight structures in TiAl6V4. online. J Laser Appl. 2015, roč. 27, č. 1, s. 14001. ISSN 1042-346X. Dostupné z: doi:https://doi.org/10.2351/1.4885235. [cit. 2022-07-26].

[4] Kučerová, Ludmila; Burdová, Karolina; Jeníček, Štěpán and Chena, Iveta. Effect of solution annealing and precipitation hardening at 250 °C–550 °C on microstructure and mechanical properties of additively manufactured 1.2709 maraging steel. online. Mater Sci Eng A, Structural materials: properties, microstructure and processing. 2021, roč. 814, s. 1. ISSN 0921-5093. Dostupné z: doi:https://doi.org/10.1016/j.msea.2021.141195. [cit. 2022-05-08].

[5] Fortunato, Alessandro; Lulaj, Amarildo; Melkote, Shreyes; Liverani, Erica; Ascari, Alessandro et al. Milling of maraging steel components produced by selective laser melting. online. Int J Adv Manuf Technol. 2017, roč. 94, č. 5–8, s. 1895–1902. ISSN 0268-3768. Dostupné z: doi:https://doi.org/10.1007/s00170-017-0922-9. [cit. 2022-04-27].

[6] Du, Wei; Bai, Qian and Zhang, Bi. Machining characteristics of 18Ni-300 steel in additive/subtractive hybrid manufacturing. online. Int J Adv Manuf Technol. 2017, roč. 95, č. 5–8, s. 2509–2519. ISSN 0268–3768. Dostupné z:doi:https://doi.org/10.1007/s00170-017-1364-0. [cit. 2022-04-27].

[7] Chen, Hongyu; Gu, Dongdong; Dai, Donghua; Ma, Chenglong and Xia, Mujian. Microstructure and composition homogeneity, tensile property, and underlying thermal physical mechanism of selective laser melting tool steel parts. online. Mat Sci Eng A, Structural materials: properties, microstructure and processing. 2017, roč. 682, s. 279–289. ISSN 0921-5093. Dostupné z: doi:https://doi.org/10.1016/j.msea.2016.11.047. [cit. 2024-04-12].

[8] Nong, X.D. and Zhou, X.L. Effect of scanning strategy on the microstructure, texture, and mechanical properties of 15-5PH stainless steel processed by selective laser melting. online. Mater Charact. 2021, roč. 174, s. 111012. ISSN 1044–5803. Dostupné z: doi:https://doi.org/10.1016/j.matchar.2021.111012. [cit. 2022-04-28].

[9] Marattukalam, Jithin; Karlsson, Dennis; Pacheco, Victor; Beran, Přemysl; Wiklund, Urban et al. The effect of laser scanning strategies on texture, mechanical properties, and site-specific grain orientation in selective laser melted 316L SS.

online. Mater Des. 2020, roč. 193, s. 108852. ISSN 0264–1275. Dostupné z: doi:https://doi.org/10.1016/j.matdes.2020.108852. [cit. 2022-04-28].
[10] Larimian, Taban; Almangour, Bandar; Grzesiak, Dariusz; Walunj, Ganesh and Borkar, Tushar. Effect of Laser Spot Size, Scanning Strategy, Scanning Speed, and Laser Power on Microstructure and Mechanical Behavior of 316L Stainless Steel Fabricated via Selective Laser Melting. online. J Mater Eng Perform. 2021, roč. 31, č. 3, s. 2205–2224. ISSN 1059–9495. Dostupné z: doi:https://doi.org/10.1007/s11665-021-06387-8. [cit. 2022-05-03].
[11] Opěla, Petr; Benč, Marek; Kolomy, Stepan; Jakůbek, Zdeněk and Beranová, Denisa. High Cycle Fatigue Behaviour of 316L Stainless Steel Produced via Selective Laser Melting Method and Post Processed by Hot Rotary Swaging. online. Materials. 2023, roč. 16, č. 9, s. 3400. ISSN 1996–1944. Dostupné z: doi:https://doi.org/10.3390/ma16093400. [cit. 2023-05-22].
[12] Wan, H.Y., Zhou, Z.J., Li, C.P., Chen, G.F. and Zhang, G.P. Effect of scanning strategy on mechanical properties of selective laser melted Inconel 718. online. Mater Sci Eng A, Structural materials: properties, microstructure and processing. 2019, roč. 753, s. 42–48. ISSN 0921–5093. Dostupné z: doi:https://doi.org/10.1016/j.msea.2019.03.007. [cit. 2022-05-03].
[13] Amirjan, Mostafa and Sakiani, Hassan. Effect of scanning strategy and speed on the microstructure and mechanical properties of selective laser melted IN718 nickel-based superalloy. online. Int J Adv Manuf Technol. 2019, roč. 103, č. 5–8, s. 1769–1780. ISSN 0268–3768. Dostupné z: doi:https://doi.org/10.1007/s00170-019-03545-0. [cit. 2022-05-03].
[14] Wan, H.Y.; Zhou, Z.J.; Li, C.P.; Chen, G.F. and Zhang, G.P.. Effect of scanning strategy on grain structure and crystallographic texture of Inconel 718 processed by selective laser melting. online. J Mater Sci Technol. 2018, roč. 34, č. 10, s. 1799–1804. ISSN 1005–0302. Dostupné z: doi:https://doi.org/10.1016/j.jmst.2018.02.002. [cit. 2022-05-03].
[15] Zhang, Xuan; Xu, Hao; Li, Zhongjie; Dong, Anping; Du, Dafan et al. Effect of the scanning strategy on microstructure and mechanical anisotropy of Hastelloy X superalloy produced by Laser Powder Bed Fusion. online. Mater Charact. 2021, roč. 173, s. 110951. ISSN 1044–5803. Dostupné z: doi:https://doi.org/10.1016/j.matchar.2021.110951. [cit. 2022-05-03].
[16] Gushchina, Marina; Kuzminova, Yulia; Kudryavtsev, Egor; Babkin, Konstantin; Andreeva, Valentina et al. Effect of Scanning Strategy on Mechanical Properties of Ti-6Al-4V Alloy Manufactured by Laser Direct Energy Deposition. online. J Mater Eng Perform. 2021, roč. 31, č. 4, s. 2783–2791. ISSN 1059–9495. Dostupné z: doi:https://doi.org/10.1007/s11665-021-06407-7. [cit. 2022-05-03].
[17] Ali, Haider; Ghadbeigi, Hassan and Mumtaz, Kamran. Effect of scanning strategies on residual stress and mechanical properties of Selective Laser Melted Ti6Al4V. online. Mater Sci Eng A, Structural materials: properties, microstructure and processing. 2018, roč. 712, s. 175–187. ISSN 0921–5093. Dostupné z: doi:https://doi.org/10.1016/j.msea.2017.11.103. [cit. 2022-05-03].
[18] Guan Jieren, Wang Qiuping. The effect of a remelting treatment scanning strategy on the surface morphology, defect reduction mechanism, and mechanical properties of a selective laser-melted Al-based alloy. online J Mater Sci 2022 ISSN: 0022-2461. https://doi.org/10.1007/s10853-021-06761-w. Dostupné z. [cit. 2022-05-03].
[19] Chen, Hongyu; Gu, Dongdong; Xiong, Jiapeng and Xia, Mujian. Improving additive manufacturing processability of hard-to-process overhanging structure by selective laser melting. online. J Mater Process Technol. 2017, roč. 250, s. 99–108. ISSN 0924–0136. Dostupné z: doi:https://doi.org/10.1016/j.jmatprotec.2017.06.044. [cit. 2024-04-12].
[20] Deirmina, Faraz; Peghini, Nicola; Almangour, Bandar; Grzesiak, Dariusz and Pellizzari, Massimo. Heat treatment and properties of a hot work tool steel fabricated by additive manufacturing. online. Mater Sci Eng A, Structural materials: properties, microstructure and processing. 2019, roč. 753, s. 109–121. ISSN 0921–5093. Dostupné z: doi:https://doi.org/10.1016/j.msea.2019.03.027. [cit. 2021-12-10].
[21] Kolomy, Stepan; Sedlak, Josef; Zouhar, Jan; Slany, Martin; Benc, Marek et al. Influence of Aging Temperature on Mechanical Properties and Structure of M300 Maraging Steel Produced by Selective Laser Melting. online. Materials. 2023, roč. 16, č. 3, s. 977. ISSN 1996–1944. Dostupné z: doi:https://doi.org/10.3390/ma16030977. [cit. 2023-01-29].
[22] Kale, Amol; Singh, Jaiveer; Kim, Byung-kyu; Kim, Dong-ik and Choi, Shi-hoon. Effect of initial microstructure on the deformation heterogeneities of 316L stainless steels fabricated by selective laser melting processing. online. J Mater Res Technol. 2020, roč. 9, č. 4, s. 8867–8883. ISSN 2238–7854. Dostupné z: doi:https://doi.org/10.1016/j.jmrt.2020.06.015. [cit. 2022-10-08].
[23] Harant, Martin; Verleysen, Patricia; Forejt, Milan and Kolomy, Stepan. The Effects of Strain Rate and Anisotropy on the Formability and Mechanical Behaviour of Aluminium Alloy 2024-T3. online. Metals (Basel). 2024, roč. 14, č. 1, s. 98. ISSN 2075–4701. Dostupné z: doi:https://doi.org/10.3390/met14010098. [cit. 2024-04-12].
[24] Segura, I.A.; Mireles, J.; Bermudez, D.; Terrazas, C.A.; Murr, L.E. et al. Characterization and mechanical properties of cladded stainless steel 316L with nuclear applications fabricated using electron beam melting. online. J Nucl Mater. 2018, roč. 507, č., s. 164–176. ISSN 0022–3115. Dostupné z: doi:https://doi.org/10.1016/j.jnucmat.2018.04.026. [cit. 2022-10-08].
[25] Viliš, Jindřich; Pokorný, Zdeněk; Zouhar, Jan and Jopek, Miroslav. Ballistic Resistance of Composite Materials Tested by Taylor Anvil Test. online. Manuf Technol. 2022, roč. 22, č. 5, s. 610–616. ISSN 12132489. Dostupné z: doi:10.21062/mft.2022.074. [cit. 2023-03-08].
[26] Lin, J.J.; Lv, Y.H.; Liu, Y.X.; Xu, B.S.; Sun, Z. et al. Microstructural evolution and mechanical properties of Ti-6Al-4V wall deposited by pulsed plasma arc additive manufacturing. online. Mater Des. 2016, roč. 102, s. 30–40. ISSN 0264–1275. Dostupné z: doi:https://doi.org/10.1016/j.matdes.2016.04.018. [cit. 2022-10-08].
[27] Rua Julian, Buchely Mario, Monteiro Sergio, Colorado Henry. Structure–Property Relation of Epoxy Resin with Fique Fibers: Dynamic Behavior Using Split-Hopkinson Pressure Bar and Charpy Tests. In: Green Materials Engineering. ISSN2367-1181. Cham: Springer International Publishing; 2019. p. 49–56. https://doi.org/10.1007/978-3-030-10383-5_5. Dostupné z.
[28] Lu, Y.B. and Li, Q.M. Dynamic behavior of polymers at high strain-rates based on split Hopkinson pressure bar tests. online. Int J Impact Eng. 2011, roč. 38, č. 1, s. 41–50. ISSN 0734-743X. Dostupné z: doi:https://doi.org/10.1016/j.ijimpeng.2010.08.001. [cit. 2022-05-04].
[29] Gilbertson Christopher G. Dynamic properties of wood using the Split-Hopkinson Pressure Bar, ISBN 1124913319.
[30] Chen, Xudong; Ge, Limei; Zhou, Jikai and Wu, Shengxing. Dynamic Brazilian test of concrete using split Hopkinson pressure bar. online. Mater Struct. 2016, roč. 50, č. 1, s. 1–15. ISSN 1359–5997. Dostupné z: doi:https://doi.org/10.1617/s11527-016-0885-6. [cit. 2022-05-04].
[31] Kang, Minju; Cho, Jung-woo; Kim, Yang; Park, Jaeyeong; Jeong, Myeong-sik et al. Dynamic compressive properties obtained from a split Hopkinson pressure bar test of Boryeong shale. online. Met Mater Int. 2016, roč. 22, č. 5, s. 764–770. ISSN 1598–9623. Dostupné z: doi:https://doi.org/10.1007/s12540-016-6096-4. [cit. 2022-05-04].
[32] Renliang, Shan; Yongwei, Song; Liwei, Song and Yao, Bai. Dynamic property tests of frozen red sandstone using a split hopkinson pressure bar. online. Earthq Eng Eng Vib. 2019, roč. 18, č. 3, s. 511–519. ISSN 1671–3664. Dostupné z: doi:https://doi.org/10.1007/s11803-019-0518-5. [cit. 2022-05-04].
[33] Li, Chengjie; Xu, Ying; Chen, Peiyuan; Li, Hailong and Lou, Peijie. Dynamic Mechanical Properties and Fragment Fractal Characteristics of Fractured Coal–Rock-Like Combined Bodies in Split Hopkinson Pressure Bar Tests. online. Nat Resour Res (New York, N.Y.). 2020, roč. 29, č. 5, s. 3179–3195. ISSN 1520–7439. Dostupné z: doi:https://doi.org/10.1007/s11053-020-09656-w. [cit. 2022-05-04].
[34] Liu, Peijie; Quan, Yanming and Ding, Guo. Dynamic Mechanical Characteristics and Constitutive Modeling of Rail Steel over a Wide Range of Temperatures and Strain Rates. online. Adv Mater Sci Eng. 2019, roč. 2019, s. 1–15. ISSN 1687–8434. Dostupné z: doi:https://doi.org/10.1155/2019/6862391. [cit. 2022-05-04].
[35] Jopek, Miroslav. Determination of Carbon Steel Dynamic Properties. online. Manuf Technol. roč. 21, č. 4, s. 479–482. ISSN 1213–2489. Dostupné z: doi:10.21062/mft.2021.061. [cit. 2022-05-04].
[36] Kunčická, Lenka; Jopek, Miroslav; Kocich, Radim and Dvořák, Karel. Determining johnson-cook constitutive equation for low-carbon steel via taylor anvil test. online. Materials. 2021, roč. 14, č. 17, s. 4821. ISSN 1996–1944. Dostupné z: doi:https://doi.org/10.3390/ma14174821. [cit. 2022-05-04].
[37] Zhang, Xueqin; Zhang, Keqiang; Zhang, Bin; Li, Ying and He, Rujie. Quasi-static and dynamic mechanical properties of additively manufactured Al2O3 ceramic lattice structures: effects of structural configuration. online. Virtual Phys Prototyp. 2022, roč. 17, č. 3, s. 528–542. ISSN 1745–2759. Dostupné z: doi:https://doi.org/10.1080/17452759.2022.2048340. [cit. 2022-05-05].
[38] Sharma, Vishal; Singh, Sharanjit; Sachdeva, Anish and Kumar, Parmod. Influence of sintering parameters on dynamic mechanical properties of selective laser sintered parts. online. Int J Mater Form. 2013, roč. 8, č. 1, s. 157–166. ISSN 1960–6206. Dostupné z: doi:https://doi.org/10.1007/s12289-013-1158-3. [cit. 2022-05-08].
[39] Mansour M, Tsongas K, Tzetzis D. Measurement of the mechanical and dynamic properties of 3D printed polylactic acid reinforced with graphene. online Polym-Plast Technol Eng 2018 ISSN: 0360-2559. https://doi.org/10.1080/03602559.2018.1542730. Dostupné z. [cit. 2022-05-05].
[40] Muiruri, Amos; Maringa, Maina and Du Preez, Willie. Numerical Simulation of High Strain Rate and Temperature Properties of Laser Powder Bed Fusion Ti6Al4V (ELI) Determined Using a Split Hopkinson Pressure Bar. online. Materials. 2022, roč. 15, č. 5, s. 1872. ISSN 1996-1944. Dostupné z: doi:https://doi.org/10.3390/ma15051872. [cit. 2022-05-04].
[41] Yang, Liu; Zhicong, Pang; Ming, Li; Yonggang, Wang; Di, Wang et al. Investigation into the dynamic mechanical properties of selective laser melted Ti-6Al-4V alloy at high strain rate tensile loading. online. Mater Sci Eng A, Structural materials: properties, microstructure and processing. 2019, roč. 745, s. 440–449. ISSN 0921–5093. Dostupné z: doi:https://doi.org/10.1016/j.msea.2019.01.010. [cit. 2022-05-08].
[42] Nurel, Bar; Nahmany, Moshe; Frage, Nachum; Stern, Adin and Sadot, Oren. Split Hopkinson pressure bar tests for investigating dynamic properties of additively manufactured AlSi10Mg alloy by selective laser melting. online. Addit Manuf. 2018, roč. 22, s. 823–833. ISSN 2214–8604. Dostupné z: doi:https://doi.org/10.1016/j.addma.2018.06.001. [cit. 2022-05-05].
[43] Amir, Ben; Grinberg, Eyal; Gale, Yuval; Sadot, Oren and Samuha, Shmuel. Experimental investigation on the effect of platform heating on the dynamic mechanical properties of selective laser manufacturing of AlSi10Mg alloy. online. EPJ Web Conf. 2021, roč. 250, s. 5016. ISSN 2100-014X. Dostupné z: doi:https://doi.org/10.1051/epjconf/202125005016. [cit. 2022-05-05].
[44] Maconachie, Tobias; Leary, Martin; Zhang, Jianjun; Medvedev, Alexander; Sarker, Avik et al. Effect of build orientation on the quasi-static and dynamic response of SLM AlSi10Mg. online. Mater Sci Eng A, Structural materials: properties, microstructure and processing. 2020, roč. 788, s. 139445. ISSN 0921–5093. Dostupné z: doi:https://doi.org/10.1016/j.msea.2020.139445. [cit. 2023-01-16].
[45] Smith Liam, Chapman David, Hooper Paul, Whiteman Glenn, Eakins Daniel. On the dynamic response of additively manufactured 316L. online. In: AIP Conference

Proceedings. ISSN0094-243X. Melville: American Institute of Physics; 2018, ISBN 0735416931. https://doi.org/10.1063/1.5044804. Dostupné z. [cit. 2022-05-05].
[46] Chen, Jie; Wei, Haiyang; Bao, Kuo; Zhang, Xianfeng; Cao, Yang et al. Dynamic mechanical properties of 316L stainless steel fabricated by an additive manufacturing process. online. J Mater Res Technol. 2021, roč. 11, s. 170–179. ISSN 2238–7854. Dostupné z: doi:https://doi.org/10.1016/j.jmrt.2020.12.097. [cit. 2022-05-05].
[47] Song Bo, Sanborn Brett, Wakeland Peter, Furnish Michael. Dynamic Characterization and Stress-Strain Symmetry of Vascomax® C250 Maraging Steel in Compression and Tension. online. In: Procedia Engineering. ISSN1877-7058. United States: Elsevier Ltd; 2017. p. 42–51. https://doi.org/10.1016/j.proeng.2017.08.080. Dostupné z. [cit. 2023-02-25].
[48] Dehgahi, S.; Alaghmandfard, R.; Tallon, J.; Odeshi, A. and Mohammadi, M. Microstructural evolution and high strain rate compressive behavior of as-built and heat-treated additively manufactured maraging steels. online. Mater Sci Eng A, Structural materials: properties, microstructure and processing. 2021, roč. 815, s. 141183. ISSN 0921–5093. Dostupné z: doi:https://doi.org/10.1016/j.msea.2021.141183. [cit. 2023-02-25].
[49] Pitassi Dario. Finite Element Thermal Analysis of Metal Parts Additively Manufactured via Selective Laser Melting. IntechOpen; 2018, ISBN 9789535138495. https://doi.org/10.5772/intechopen.71876. Dostupné z.
[50] Thijs, Lore; Verhaeghe, Frederik; Craeghs, Tom; Humbeeck, Jan and Kruth, Jean-pierre. A study of the microstructural evolution during selective laser melting of Ti–6Al–4V. online. Acta Mater. 2010, roč. 58, č. 9, s. 3303–3312. ISSN 1359–6454. Dostupné z: doi:https://doi.org/10.1016/j.actamat.2010.02.004. [cit. 2022-07-26].
[51] Bhardwaj, Tarun and Shukla, Mukul. Effect of laser scanning strategies on texture, physical and mechanical properties of laser sintered maraging steel. online. Mater Sci Eng A, Structural materials: properties, microstructure and processing. 2018, roč. 734, s. 102–109. ISSN 0921-5093. Dostupné z: doi:https://doi.org/10.1016/j.msea.2018.07.089. [cit. 2022-07-26].
[52] Naftaly, Mira; Savvides, Gian; Alshareef, Fawwaz; Flanigan, Patrick; Lui, Gianluc et al. Non-Destructive Porosity Measurements of 3D Printed Polymer by Terahertz Time-Domain Spectroscopy. online. Dostupné z: doi:https://doi.org/10.3390/app12020927. [cit. 2023-01-29].
[53] Yao, Yi; Wang, Kaiwen; Wang, Xiaoqing; Li, Lin; Cai, Wenjun et al. Microstructural heterogeneity and mechanical anisotropy of 18Ni-330 maraging steel fabricated by selective laser melting: The effect of build orientation and height. online. J Mater Res. 2020, roč. 35, č. 15, s. 2065–2076. ISSN 0884–2914. Dostupné z: doi:https://doi.org/10.1557/jmr.2020.126. [cit. 2022-04-28].
[54] Król, Mariusz; Snopiński, Przemysław; Hajnyš, Jiří; Pagáč, Marek and Łukowiec, Dariusz. Selective laser melting of 18Ni-300 maraging steel. online. Materials. 2020, roč. 13, č. 19, s. 4268. ISSN 1996–1944. Dostupné z: doi:https://doi.org/10.3390/MA13194268. [cit. 2022-05-08].
[55] Wang, Pan; Huang, Pengfei; Ng, Fern; Sin, Wai; Lu, Shenglu et al. Additively manufactured CoCrFeNiMn high-entropy alloy via pre-alloyed powder. online. Mater Des. 2019, roč. 168, s. 107576. ISSN 0264–1275. Dostupné z: doi:https://doi.org/10.1016/j.matdes.2018.107576. [cit. 2022-10-07].
[56] Wang, Pan; Song, Jie; Nai, Mui and Wei, Jun. Experimental analysis of additively manufactured component and design guidelines for lightweight structures: A case study using electron beam melting. online. Addit Manuf. 2020, roč. 33, s. 101088. ISSN 2214–8604. Dostupné z: doi:https://doi.org/10.1016/j.addma.2020.101088. [cit. 2022-10-07].
[57] Kaynak, Yusuf and Kitay, Ozhan. Porosity, surface quality, microhardness and microstructure of selective laser melted 316l stainless steel resulting from finish machining. online. J Manuf Mater Process. 2018, roč. 2, č. 2, s. 36. ISSN 2504–4494. Dostupné z: doi:https://doi.org/10.3390/jmmp2020036. [cit. 2022-04-27].
[58] Kunčická, Lenka; Kocich, Radim; Németh, Gergely; Dvořák, Karel and Pagáč, Marek. Effect of post process shear straining on structure and mechanical properties of 316 L stainless steel manufactured via powder bed fusion. online. Addit Manuf. 2022, roč. 59, s. 103128. ISSN 2214–8604. Dostupné z: doi:https://doi.org/10.1016/j.addma.2022.103128. [cit. 2023-01-03].
[59] Bai, Yuchao; Yang, Yongqiang; Wang, Di and Zhang, Mingkang. Influence mechanism of parameters process and mechanical properties evolution mechanism of maraging steel 300 by selective laser melting. online. Mater Sci Eng A, Structural materials: properties, microstructure and processing. 2017, roč. 703, s. 116–123. ISSN 0921–5093. Dostupné z: doi:https://doi.org/10.1016/j.msea.2017.06.033. [cit. 2022-05-08].
[60] Rigon, Daniele; Meneghetti, Giovanni; Görtler, Michael; Cozzi, Daniele; Waldhauser, Wolfgang et al. Influence of defects on axial fatigue strength of maraging steel specimens produced by additive manufacturing. online. MATEC Web Conf. 2018, roč. 165, s. 2005. ISSN 2261-236X. Dostupné z: doi:https://doi.org/10.1051/matecconf/201816502005. [cit. 2022-05-09].
[61] Deirmina, Faraz; Peghini, Nicola; Almangour, Bandar; Grzesiak, Dariusz and Pellizzari, Massimo. Heat treatment and properties of a hot work tool steel fabricated by additive manufacturing. online. Mater Sci Eng A, Structural materials: properties, microstructure and processing. 2019, roč. 753, s. 109–121. ISSN 0921–5093. Dostupné z: doi:https://doi.org/10.1016/j.msea.2019.03.027. [cit. 2023-02-05].
[62] Mazumder, J.; Choi, J.; Nagarathnam, K.; Koch, J. a Hetzner, D. The direct metal deposition of H13 tool steel for 3-D components. online. JOM (1989). 1997, roč. 49, č. 5, s. 55–60. ISSN 1047–4838. Dostupné z: doi:https://doi.org/10.1007/BF02914687. [cit. 2023-02-19].
[63] Dvorský, Drahomír; Strakosova, Angelina and Vojtech, Dalibor. Heat Treatment of High-Strength 3D-Printed Maraging Steel. online. Diffusion and defect data. Solid state data. Pt. A, Defect and diffusion forum. 2020, roč. 403, s. 67–73. ISSN 1012–0386. Dostupné z: doi:https://doi.org/10.4028/www.scientific.net/DDF.403.67. [cit. 2022-05-08].
[64] Prasad, Kartik; Obana, Mitsuki; Ishii, Yuki; Ito, Atsushi and Torizuka, Shiro. The effect of laser scanning strategies on the microstructure, texture and crystallography of grains exhibiting hot cracks in additively manufactured Hastelloy X. online. Mech Mater. 2021, roč. 157, s. 103816. ISSN 0167–6636. Dostupné z: doi:https://doi.org/10.1016/j.mechmat.2021.103816. [cit. 2022-05-03].
[65] Sun, Shi-hai; Hagihara, Koji and Nakano, Takayoshi. Effect of scanning strategy on texture formation in Ni-25 at.%Mo alloys fabricated by selective laser melting. online. Mater Des. 2018, roč. 140, s. 307–316. ISSN 0264–1275. Dostupné z: doi:https://doi.org/10.1016/j.matdes.2017.11.060. [cit. 2022-05-03].
[66] Thijs, Lore; Montero Sistiaga, Maria; Wauthle, Ruben; Xie, Qingge; Kruth, Jean-pierre et al. Strong morphological and crystallographic texture and resulting yield strength anisotropy in selective laser melted tantalum. online. Acta Mater. 2013, roč. 61, č. 12, s. 4657–4668. ISSN 1359–6454. Dostupné z: doi:https://doi.org/10.1016/j.actamat.2013.04.036. [cit. 2023-02-24].
[67] Dehoff, R.; Kirka, M.; Sames, W.; Bilheux, H.; Tremsin, A. et al. Site specific control of crystallographic grain orientation through electron beam additive manufacturing. online. Dostupné z: doi:https://doi.org/10.1179/1743284714Y.0000000734. [cit. 2023-02-24].